Trans-rectal ultrasound-coupled near-infrared optical tomography of the prostate Part II: Experimental demonstration

Zhen Jiang,[1] Daqing Piao,[1*] Guan Xu,[1] Jerry W. Ritchey,[2] G. Reed Holyoak,[3] Kenneth E. Bartels,[3] Charles F. Bunting,[1] Gennady Slobodov,[4] Jerzy S. Krasinki [1]

[1] *School of Electrical and Computer Engineering, Oklahoma State University, Stillwater, OK 74078 USA*
[2] *Department of Veterinary Pathobiology, Oklahoma State University, Stillwater, OK 74078 USA*
[3] *Department of Veterinary Clinical Sciences, Oklahoma State University, Stillwater, OK 74078 USA*
[4] *Department of Urology, University of Oklahoma Health Science Center, Oklahoma City, OK 73104 USA*
[*] *Corresponding author: daqing.piao@okstate.edu*

Abstract: We demonstrate trans-rectal optical tomography of the prostate using an endo-rectal near-infrared (NIR) applicator integrated with a trans-rectal ultrasound (TRUS) probe. The endo-rectal NIR applicator incorporated a design presented in our previously reported work. A continuous-wave NIR optical tomography system is combined with a commercial US scanner to form the dual-modality imager. Sagittal trans-rectal imaging is performed concurrently by endo-rectal NIR and TRUS. The TRUS ensures accurate positioning of the NIR applicator as well as guides NIR image reconstruction using the spatial prior of the target. The use of a condom, which is standard for TRUS, is found to have minimal effect on trans-rectal NIR imaging. Tests on avian tissues validates that NIR imaging can recover the absorption contrast of a target, and its accuracy is improved when the TRUS spatial prior is incorporated. Trans-rectal NIR/US imaging of a healthy canine prostate in situ is reported.

OCIS codes: (170.3880) Medical and biological imaging; (170.6960) Tomography; (170.7230) Urology; (170.1610) Clinical applications.

References and links

1. G. Xu, D. Piao, C. H. Musgrove, C. F. Bunting, and H. Dehghani, "Trans-rectal ultrasound coupled trans-rectal optical tomography of the prostate Part I: Simulations," Accepted for publication in Opt. Express.
2. G. D. Grossfeld and P. R. Carroll, "Prostate cancer early detection: a clinical perspective," Epidemiol. Rev. **23**, 173-80 (2001).
3. A. C. Loch, A. Bannowsky, L. Baeurle, B. Grabski, B. König, G. Flier, O. Schmitz-Krause, U. Paul, and T. Loch, "Technical and anatomical essentials for transrectal ultrasound of the prostate," World J. Urol. **25**, 361-366 (2007).
4. C. R. Porter, "Does the number of prostate biopsies performed affect the nature of the cancer identified?" Nat. Clin. Pract. Urol. **4**, 132-133 (2007).
5. V. Scattoni, A. Zlotta, R. Montironi, C. Schulman, P. Rigatti, and F. Montorsi, "Extended and saturation prostatic biopsy in the diagnosis and characterisation of prostate cancer: a critical analysis of the literature," Eur. Urol. **52**,1309-1322 (2007).
6. B. Spajic, H. Eupic, D. Tomas, G. Stimac, B. Kruslin, and O. Kraus, "The incidence of hyperechoic prostate cancer in transrectal ultrasound-guided biopsy specimens," Urology **70**, 734-737 (2007).
7. K. Shinohara, T. M. Wheeler, and P. T. Scardino, "The appearance of prostate cancer on transrectal ultrasonography: correlation of imaging and pathological examinations," J. Urol. **142**, 76-82 (1989).
8. B. Tromberg, J. Coquoz, O. Fishkin, J. B. Pham, T. Anderson, E. R. Butler, J. Cahn, M. Gross, J. D. Venugopalan, and D. Pham, "Non-invasive measurements of breast tissue optical properties using frequency-domain photon migration," Phil. Trans. R. Soc. Lond. B **352**, 661-668 (1997).
9. B. W. Pogue, S. P. Poplack, T. O. McBride, W. A. Wells, K. S. Osterman, U. L. Osterberg, and K. D. Paulsen," Quantitative hemoglobin tomography with diffuse near-infrared spectroscopy: pilot results in the breast," Radiology **218**, 261-266 (2001).

#99971 - $15.00 USD Received 8 Aug 2008; revised 13 Oct 2008; accepted 14 Oct 2008; published 15 Oct 2008

10. V. Ntziachristos and B. Chance, "Probing physiology and molecular function using optical imaging: applications to breast cancer," Breast Cancer Res. **3**, 41-46 (2001).
11. R. Choe, A. Corlu, K. Lee, T. Durduran, S. D. Konecky, M. Grosicka-Koptyra, S. R. Arridge, B. J. Czerniecki, D. L. Fraker, A. DeMichele, B. Chance, M. A. Rosen, and A. G. Yodh, "Diffuse optical tomography of breast cancer during neoadjuvant chemotherapy: a case study with comparison to MRI," Med. Phys. **32**, 1128-1139 (2005).
12. M. A. Franceschini, K. T. Moesta, S. Fantini, G. Gaida, E. Gratton, H. Jess, W. W. Mantulin, M. Seeber, P. M. Schlag, and M. Kaschke, "Frequency-domain techniques enhance optical mammography: initial clinical results," Proc. Nat. Acad. Sci. USA **94**, 6468-6473 (1997).
13. Q. Zhu, E. B. Cronin, A. A. Currier, H. S. Vine, M. Huang, N. Chen, and C. Xu, "Benign versus malignant breast masses: optical differentiation with US-guided optical imaging reconstruction," Radiology **237**, 57-66 (2005).
14. B. J. Tromberg, B. W. Pogue, K. D. Paulsen, A. G. Yodh, D. A. Boas, and A. E. Cerussi, "Assessing the future of diffuse optical imaging technologies for breast cancer management," Med Phys. **35**, 2443-51 (2008).
15. J. H. Ali , W. B. Wang , M. Zevallos, and R. R. Alfano , "Near infrared spectroscopy and imaging to probe differences in water content in normal and cancer human prostate tissues," Technol. Cancer Res. Treat. **3**, 491-497 (2004).
16. M. R. Arnfield , J. D. Chapman, J. Tulip, M. C. Fenning, and M. S. McPhee, "Optical properties of experimental prostate tumors in vivo," Photochem. Photobiol. **57**, 306-311 (1993).
17. T. C. Zhu, A. Dimofte, J. C. Finlay, D. Stripp, T. Busch, J. Miles, R. Whittington, S. B. Malkowicz, Z. Tochner, E. Glatstein, and S. M. Hahn, "Optical properties of human prostate at 732 nm measured in mediated photodynamic therapy," Photochem. Photobiol. **81**, 96-105 (2005).
18. T. Svensson, S. Andersson-Engels, M. Einarsdóttír, and K. Svanberg, "In vivo optical characterization of human prostate tissue using near-infrared time-resolved spectroscopy," J. Biomed. Opt. **12**, 014022 (2007).
19. M. Goel, H. Radhakrishnan, H. Liu, et al. "Application of near infrared multi-spectral CCD imager system to determine the hemodynamic changes in prostate tumor," in *OSA Biomedical Topical Meetings* (Optical Society of America, 2006), paper SH10.
20. X. Zhou and T. C. Zhu, "Image reconstruction of continuous wave diffuse optical tomography (DOT) of human prostate," in *Proc. the COMSOL Users Conference* (2006) .
21. S. L. Jacques and M. Motamedi, "Tomographic needles and catheters for optical imaging of prostatic cancer," Proc. SPIE **2395**, 111-118 (1995).
22. C. Li, R. Liengsawangwong, H. Choi, and R. Cheung , "Using *a priori* structural information from magnetic resonance imaging to investigate the feasibility of prostate diffuse optical tomography and spectroscopy: a simulation study," Med. Phys. **34**, 266-274 (2007).
23. H. Dehghani, C. M. Carpenter, P. K. Yalavarthy, B. W. Pogue, and J. P. Culver, "Structural *a priori* information in near-infrared optical tomography," Proc. SPIE **6431**, 64310B1-7 (2007).
24. M. J. Holboke, B. J. Tromberg, X. Li, N. Shah, J. Fishkin, D. Kidney, J. Butler, B. Chance, and A. G. Yodh, "Three-dimensional diffuse optical mammography with ultrasound localization in a human subject," J. Biomed Opt. **5,** 237-247 (2000).
25. A. Li, E. L. Miller, M. E. Kilmer, T. J. Brukilacchio, T. Chaves, J. Stott, Q. Zhang, T. Wu, M. Chorlton, R. H. Moore, D. B. Kopans, and D. A. Boas, "Tomographic optical breast imaging guided by three-dimensional mammography," Appl. Opt. **42**, 5181-90 (2003).
26. M. Guven, B. Yazici, X. Intes, and B. Chance, "Diffuse optical tomography with a priori anatomical information," Phys. Med. Biol. **50**, 2837-58 (2005).
27. D. Piao, H. Xie. W. Zhang, J. S. Kransinski, G. Zhang, H. Dehghani, and B. W. Pogue, "Endoscopic, rapid near-infrared optical tomography," Opt. Lett. **31**, 2876-2878 (2006).
28. N. Iftimia and H. Jiang, "Quantitative optical image reconstruction of turbid media by use of direct-current measurements," Appl. Opt. **39**, 5256-5261 (2000).
29. V. Ntziachristos, "Concurrent diffuse optical tomography, spectroscopy and magnetic resonance imaging of breast cancer," PhD Dissertation, University of Pennsylvania, Philadelphia, PA, 15-16 (2000).
30. R. C. Haskell, L. O. Svaasand, T. T. Tsay, T. C. Feng, M. S. McAdams, B. J. Tromberg, "Boundary conditions for the diffusion equation in radiative transfer," J. Opt. Soc. Am. A. **11**, 2727-41 (1994).
31. R. Aronson, "Boundary conditions for diffusion of light," J. Opt. Soc. Am. A. 12, 2532-9 (1995).
32. D. Piao and B. W. Pogue, "Rapid near-infrared tomography for hemodynamic imaging using a low coherence wideband light source", J. Biomed. Opt. **12**, 014016 (2007).
33. H. Xu, "MRI-coupled broadband near-infrared tomography for small animal brain studies," Ph.D. Dissertation, Dartmouth College, Hanover, NH, 36–36 (2005).
34. S. Arridge, M. Cope, and D. Delpy, "The theoretical basis for the determination of optical pathlengths in tissue: temporal and frequency analysis," Phys. Med. Biol. Vol. 37, No **7**, 1531-1560 (1992).
35. W. F. Cheong, S. A. Prahl, and A. J. Welch, "A review of the optical properties of biological tissues," IEEE J. Quantum Electron. **26**, 2166-2185 (1990).
36. H. Xie, "Dual-spectral endoscopic near-infrared optical tomography for assessment of hemoglobin concentration and oxygen saturation," Master Thesis, Oklahoma State University (2008).

#99971 - $15.00 USD Received 8 Aug 2008; revised 13 Oct 2008; accepted 14 Oct 2008; published 15 Oct 2008

37. A. H. Hielscher, R. E. Alcouffe, and R. L. Barbour, "Comparison of finite-difference transport and diffusion calculations for photon migration in homogeneous and heterogeneous tissues," Phys. Med. Biol. **43**, 1285-302 (1998).
38. Z. Yuan, Q. Zhang, E. Sobel, and H. Jiang, "Three-dimensional diffuse optical tomography of osteoarthritis: initial results in the finger joints," J. Biomed. Opt. **12**, 034001 (2007).
39. A. Custo, W. M. Wells 3rd, A. H. Barnett, E. M. Hillman, and D. A. Boas, "Effective scattering coefficient of the cerebral spinal fluid in adult head models for diffuse optical imaging," Appl. Opt. **45**, 4747-55 (2006).
40. C. Xu, Q. Zhu, "Estimation of chest-wall-induced diffused wave distortion with the assistance of ultrasound," Appl. Opt. **44**, 4255-64 (2005).

1. Introduction

This is a continuation of previously reported work [1] whose objective is to demonstrate the feasibility of trans-rectal ultrasound (TRUS) coupled trans-rectal near-infrared (NIR) tomography of the prostate.

Prostate cancer screening is performed by measurement of serum prostate-specific antigen (PSA), digital rectal examination (DRE), and a combination of these tests [2]. When the suspicion of prostate cancer is raised by abnormal PSA and/or DRE, the diagnosis is made by biopsy performed under US guidance (most often by TRUS). Biopsy is also used to confirm neoplastic lesions and to determine their clinical significance for treatment planning [3]. The current standard of prostate biopsy is to routinely use 10 to 12 cores of tissue obtained throughout the prostate for the initial assessment [4]. It should be noted that the majority of biopsies are found to be negative, and in men with persistent suspicion of prostate cancer after several negative biopsies, more extensive protocols (>12 cores) up to saturation biopsy (24 cores) represent a necessary diagnostic procedure [5]. TRUS-guided prostate biopsy is performed following a "systematic sampling" strategy because less than 60% of neoplastic lesions appear hypoechoic on TRUS while most of the remaining neoplastic lesions appear isoechoic [6]. Also, TRUS does not reliably differentiate neoplastic from benign tumors [7].

We have suggested [1] that the accuracy of prostate biopsy may be improved if the TRUS imaging could be augmented with a functional or "surrogate" marker of a prostate tumor. Based on decades of research on cancer imaging [8-14] and prostate measurements [15-22], near-infrared (NIR) tomography, being non-ionizing and minimally-invasive similar to TRUS, has the potential of providing such functional or "surrogate" markers of prostate tumors. NIR optical tomography, if carried out trans-rectally, may improve the specificity of TRUS imaging such that prostate biopsies could be directed to the most suspicious lesions.

In the first paper of this two part series [1] we discussed the challenges of trans-rectal optical tomography, particularly the fabrication of an endo-rectal NIR applicator for integrating with TRUS. Specifically, since a TRUS-coupled endo-rectal NIR applicator requires deploying many optodes in a very limited space. We suggested [1] that arranging optodes longitudinally is feasible and the configuration would allow interrogating deep prostate tissue in a sagittal imaging geometry. Coupling endo-rectal NIR to TRUS obtains functional information otherwise unavailable from TRUS alone. Coupling endo-rectal NIR to TRUS also renders accurate and real-time anatomic information from TRUS with which to correlate NIR. The structural information obtained from TRUS may further provide the needed spatial *prior* [14, 23-26] to improve the accuracy of NIR image reconstruction. In that initial paper we further suggested [1] an array configuration of the endo-rectal NIR applicator for direct integration with a TRUS transducer.

The work presented here details the development of an endo-rectal NIR probe built on our previous work [1] and demonstrates TRUS-coupled trans-rectal NIR tomography of the prostate. It validates that trans-rectal NIR tomography helps characterize a target identified by TRUS, and the accuracy of quantitative imaging of a target by trans-rectal NIR tomography is improved when the TRUS spatial *prior* is incorporated. TRUS-coupled trans-rectal optical

#99971 - $15.00 USD Received 8 Aug 2008; revised 13 Oct 2008; accepted 14 Oct 2008; published 15 Oct 2008

tomography of a canine prostate *in situ* is performed, indicating the utility of this approach for *in vivo* imaging.

2. Instrumentation

2.1 Development of a TRUS-coupled NIR applicator for trans-rectal optical tomography

The integrated sagittal-imaging trans-rectal NIR/US applicator consists of a custom-built NIR probe and a commercial bi-plane TRUS transducer, as shown in Fig. 1. The bi-plane TRUS probe is equipped with a proximal 7.5MHz sagittal-imaging transducer and a distal 5MHz transverse-imaging transducer. The sagittal TRUS transducer occupies a 60mm×10mm window. The diameters of the sagittal and transverse imaging sections of the TRUS probe are 18mm and 20mm, respectively. Adapting to the un-even TRUS cross-section, the NIR applicator is fabricated to a cap-shape and attached to the TRUS probe (Fig. 1(a) ~(e)). The NIR array substrate was machined from a black polycarbonate material to minimize the surface reflection. This substrate was then connected to an aluminum bracket and securely fastened to the TRUS handle using a bottom clamp. The rectangular TRUS handle (Fig. 1(f) ~(g)) ensured aligning the NIR applicator to the TRUS transducer. A slot of 60mm×10mm was opened up in the NIR applicator to expose the sagittal TRUS transducer.

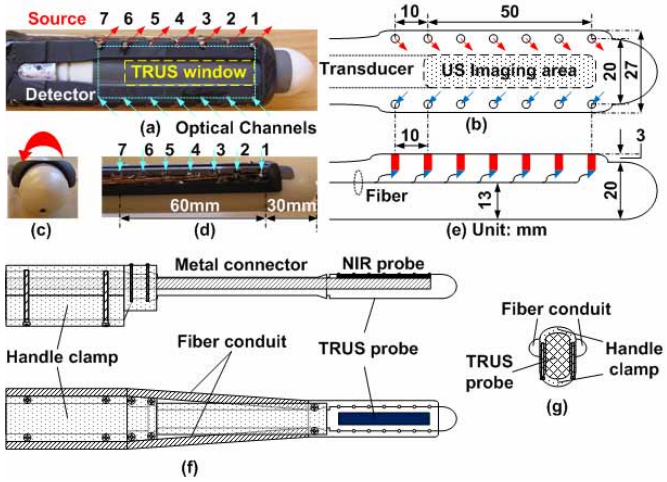

Fig. 1. The combined trans-rectal NIR/US probe: (a) top-view; (b) top-view dimension; (c) front-view; (d) side-view; (e) side-view dimension; (f) side and top views of the NIR/US alignment method; (g) rear-view of the NIR/US alignment method.

The geometry of the NIR array follows the design we previously described [1]. The NIR probe consists of two linear-arrays, one for the source and the other for the detector, separated by 20mm and placed on each side of the sagittal TRUS transducer. Each linear-array consists of 7 channels spaced 10mm apart and covering 60mm in length. The 60mm long NIR array is aligned precisely with the 60mm window of the sagittal TRUS transducer. The sagittal TRUS transducer actually has a longitudinal field-of-view (FOV) of 50mm. Therefore the NIR channels 1 to 6 on each linear-array match with the length of the sagittal TRUS transducer, and the NIR channel 7 of each linear-array is displaced longitudinally 10mm from the sagittal TRUS transducer.

A metal-coated 600μm-core diameter fiber (Oxford Electronics) is chosen for its thin cladding and mechanical strength. The 7 fibers of each linear-array are packaged into one groove of ~4mm×4mm in cross-section formed in the black substrate. Bending the fiber inside the small groove for side-firing at the probe surface is impractical. Instead micro-optics components are used for deflecting the light side-ways. As shown in Fig. 2, each source channel includes 2 gradient-index (GRIN) lenses and 1 prism attached to the fiber while each

#99971 - $15.00 USD Received 8 Aug 2008; revised 13 Oct 2008; accepted 14 Oct 2008; published 15 Oct 2008

detector channel has 1 GRIN lens and 1 prism attached to the fiber. The GRIN lens (Newport Corporation) has a pitch of 0.25, a diameter of 1mm, a length of 2.61mm, and a numerical aperture of 0.46. The prism is a coated 1mm right angle micro-prism (Tower Optics). Each fiber is polished and epoxied to a prism and a GRIN lens is attached to the other side of the micro-prism for illumination and detection at the probe surface. Each source channel has one GRIN lens attached to the proximal end of the fiber for coupling the emission of a superluminescent diode (SLD) using a spread-spectral-encoding configuration [27]. It is shown by ZEMAX (ZEMAX Development Co.) simulation that for collimated incident beam using a GRIN lens and a prism gives 38% more coupling than without the GRIN lens for a micro-prism of 80% reflection at NIR band that is typical for enhanced aluminum coating. A coupling efficiency improvement of 10%~15% is observed experimentally from the completed fiber channels. The overall coupling efficiencies of the 14 home-assembled fiber channels are shown in Table 1. The coupling efficiency is at about 50%, which could be improved if the assembly can be made more precise.

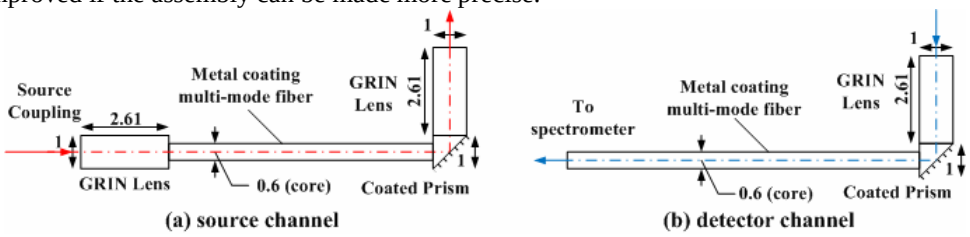

Fig. 2. Micro-optical configurations: (a) source channel; (b) detector channel. Unit: mm

Table 1. Measured coupling efficiency of the source/detector fiber channels

Source channels	s1	s2	s3	s4	s5	s6	s7
Coupling efficiency	46%	48%	49%	49%	51%	43%	49%
Detector channels	d1	d2	d3	d4	d5	d6	d7
Coupling efficiency	54%	48%	49%	51%	53%	52%	50%

2.2 Development of a continuous-wave NIR imager for coupling with US

The combined trans-rectal NIR/US imager is schematically illustrated in Fig. 3(a) and the photograph is given in Fig. 3(b). The US scanner is an ALOKA SSD-900V portable machine. The US images are transferred to the main computer of the combined imager by a PCI image acquisition card (National Instruments PCI-1405). The NIR imager uses a custom-designed superluminescent diode (SLD) (Superlumdiodes Inc.) that is pigtailed to a multi-mode fiber

#99971 - $15.00 USD Received 8 Aug 2008; revised 13 Oct 2008; accepted 14 Oct 2008; published 15 Oct 2008

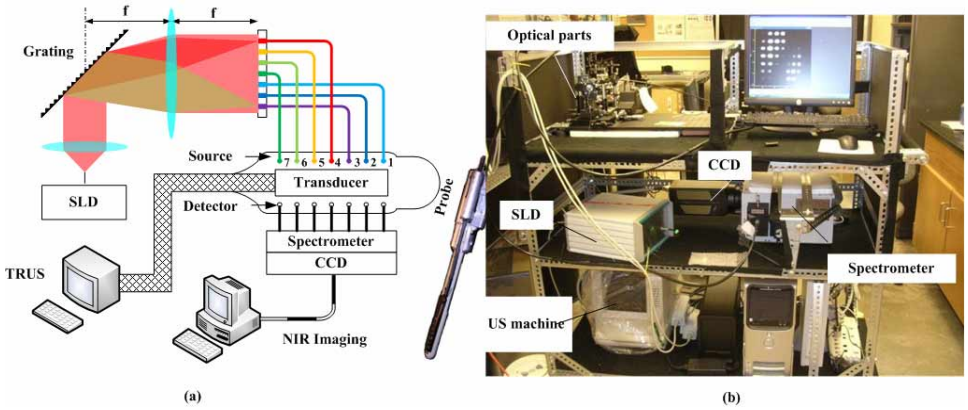

Fig. 3. The combined trans-rectal NIR/US system: (a) System diagram; (b) Photo of the system on a custom designed three-layer cart.

and delivers 100mW of 840nm NIR light with 14.2nm FWHM bandwidth. The SLD output beam is dispersed by a 1200 groves/mm grating and collimated unto linearly aligned 7 fibers connecting to the source channels on NIR applicator. NIR light with slightly different wavelengths are coupled to the 7 fibers to form a spread-spectral-encoding of the source channels [27]. The remitted lights collected by the 7 detection channels are coupled to a spectrometer (Acton Research). The signal corresponding to the individual source channels are discriminated horizontally by the spectrometer. The signals corresponding to the individual detector channels are differentiated vertically based on the position of the detection channels on the spectrometer entrance slit. A 16-bit intensified CCD camera (Princeton Instruments) acquires a complete set of NIR imaging data. The exposure time for one frame of data is in the range of 100s milliseconds, depending on the medium being imaged. The NIR system resides on a custom-built cart that also houses the US scanner.

The CCD has a maximum dynamic range of 48dB, which may not be sufficient to accommodate the full dynamic range of the signals when a medium is highly absorptive, as the minimum and maximum source-detector distances of the trans-rectal NIR array are 20mm and 63mm, respectively. Fortunately, the layout of the dual-line NIR array leads to lesser signal dynamic range for the light illuminated from the sources at the middle portion of the array than the ones at the edges of the array. Reducing the total dynamic range of the signal is possible by proper use of the Gaussian spectrum of the SLD source. The actual light coupling configuration is given in Fig. 4(a), where the stronger spectral components are coupled to the peripheral NIR channels (such as 1 and 7), and the weaker spectral components are coupled to the middle NIR channels (such as 3-5). Comparing with the configuration of coupling the uniform light to all 7 source channels, the strategy in Fig. 4(a) offers a 15dB reduction of the overall signal dynamic range for a medium of 0.0023mm^{-1} absorption coefficient and 1.0mm^{-1} reduced scattering coefficient (equivalent to a 1% Intralipid solution).

#99971 - $15.00 USD Received 8 Aug 2008; revised 13 Oct 2008; accepted 14 Oct 2008; published 15 Oct 2008

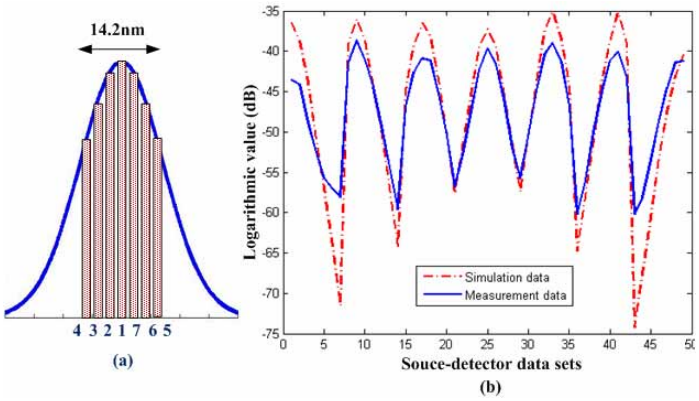

Fig. 4. Source coupling sequence with the Gaussian-spectrum (a), and the received signal dynamic range compared with the case when source channels have even intensities (b).

3. NIR image reconstruction based on continuous-wave data

The steady-state diffusion equation for a photon density U at position $\vec{r}$ can be stated as [28]

$$\nabla \cdot D(\vec{r})\nabla U(\vec{r}) - \mu_a(\vec{r}) \cdot U(\vec{r}) = -S(\vec{r}) \tag{1}$$

where μ_a is the absorption coefficient, $D = \left[3(\mu_a + \mu_s')\right]^{-1}$ is the diffusion coefficient with μ_s' being the reduced scattering coefficient, and S is a source term. For a collimated source and a detector at a semi-infinite boundary, the diffuse reflectance may be described by [29]

$$U(\rho) = \frac{S}{4\pi D\rho^2}\left[-4\left(\mu_a / D\right)^{1/2}\left(z_b^2 + z_b/\mu_s'\right)\right] \cdot \exp\left[-\left(\mu_a / D\right)^{1/2}\rho\right] \tag{2}$$

where ρ is the source-detector distance, and z_b is a length term determined by the refractive index mismatch on the boundary [30, 31].

The raw data acquired by CCD is show in Fig. 5(a). If the SLD spectral components were coupled orderly to the source channels from 1 to 7, the higher intensity signals would have been located along a diagonal line in the CCD acquired image [27, 32]. The modified source coupling configuration described in Fig. 4 leads to the pattern of diagonal-shifted high-intensity signals as shown in Fig. 5(a).

The signal non-uniformity among all source-detector pairs is calibrated using the 1% bulk Intralipid solution based on the linear relationship between $\ln\left[\rho^2 U(\rho)\right]$ and ρ derived from Eq. (2), as shown in Fig. 5(b). One calibrated data set corresponding to the complete 7×7 source-detector pairs is displayed in (c) in comparison to the non-calibrated one.

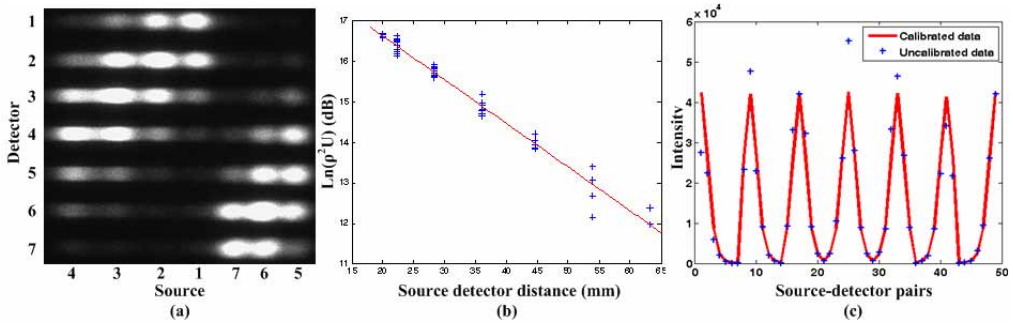

Fig. 5. Data Calibration: (a) raw CCD data; (b) linear fitting of the measurement data based on the semi-infinite model; (c) calibrated data for the signal corresponding to the 49 source-detector pairs.

#99971 - $15.00 USD Received 8 Aug 2008; revised 13 Oct 2008; accepted 14 Oct 2008; published 15 Oct 2008

Recent studies have demonstrated that absorption and reduced scattering coefficients can be reconstructed quantitatively from steady-state measurements, by updating the D and μ_a distributions to minimize a weighted sum of the squared difference between computed and measured data [28]. The method is equivalent to performing the same minimization by mapping the DC signal to frequency-domain [33], which we utilize in the reconstruction.

The frequency-domain diffusion equation [34]

$$\nabla \cdot D(\vec{r})\nabla U(\vec{r},\omega) - \left(\mu_a(\vec{r}) + \frac{i\omega}{c}\right)\cdot U(\vec{r},\omega) = -S(\vec{r},\omega) \tag{3}$$

where ω is the source modulation frequency, is used to map the Equ. (2) using finite-element discretization by setting ω to a small value of 0.1Hz. The optical properties are updated by using

$$x_{k+1} = x_k + \alpha \cdot [J^T(x_k)J(x_k) + \lambda I]^{-1} J^T(x_k)\Delta v(x_k) \tag{4}$$

where x is the parameters to be optimized, J is the Jacobian derived from Equ. (3), Δv is the forward projection error, λ is a penalty or regularization term. A small damping factor α in the range of (0, 1) is introduced to stabilize the convergence [1].

Both absorption and reduced scattering coefficients can be reconstructed from the DC measurement, but it is noted that it appears to be generally more difficult for the scattering image to be reconstructed than the absorption image [28]. In this work we focus on recovering targets having absorption contrast to demonstrate the feasibility of TRUS-coupled endo-rectal NIR optical tomography.

The geometry used for image reconstruction is illustrated in Fig. 6. The NIR image reconstruction uses a 3-dimensional mesh representing 80×40×60mm^3. The TRUS sagittal imaging is performed at the mid-plane of the NIR mesh. The TRUS image is used to develop a mesh with target spatial information. The NIR image is reconstructed in 3-dimension, and displayed at the mid-sagittal plane to correlate with TRUS image. The image reconstruction typically takes ~10 minutes on a 3.0GHz Pentium(R) 4 PC for 10 iterations.

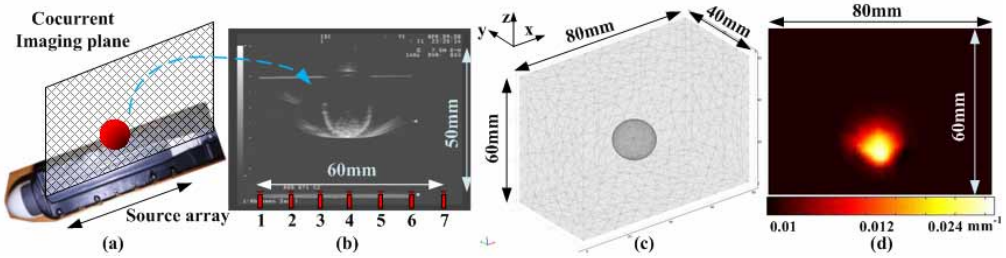

Fig. 6. NIR Imaging geometry: (a) NIR arrays are parallel and symmetric to the TRUS sagittal plane; (b) the positions of NIR channels with respect to the TRUS image; (c) mesh for NIR image reconstruction generated by use of TRUS image; (d) absorption image reconstructed from a simulation data for an absorbing target.

4. Performance evaluation for the TRUS-coupled trans-rectal NIR tomography

4.1 Imaging single target

The performance of phantom imaging by the endo-rectal NIR applicator was evaluated without the use of TRUS *prior*. A 1% bulk Intralipid solution was the background medium. A cylinder-shape solid phantom 15mm in diameter and 25mm long (Fig. 7(a)) was the target. The solid phantom was fabricated from a bulk material that was provided and calibrated by the NIR imaging laboratory of Dartmouth College. The solid phantom has an absorption

#99971 - $15.00 USD Received 8 Aug 2008; revised 13 Oct 2008; accepted 14 Oct 2008; published 15 Oct 2008

coefficient of 0.0056mm^{-1} and a reduced scattering coefficient of 1.03mm^{-1}, in comparison to 0.0023mm^{-1} and 1.0mm^{-1} of the background. The testing setup is depicted in Fig. 7(b).

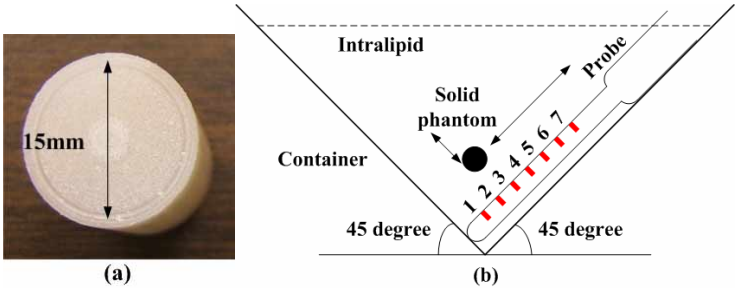

Fig. 7. Solid tissue phantom (a) and experimental setup (b)

Figure 8 lists the images reconstructed without the TRUS *prior* by using a mesh of homogenous density throughout the entire NIR imaging volume. When this mesh is used for reconstruction based on only the NIR information, the optical properties are certainly updated element-by-element in order to recover the heterogeneity being imaged. The solid phantom is placed at the mid-sagittal plane. The NIR images are displayed with a FOV of 80×30mm^2. The left most optode is located at 10mm right to the left edge of the image, and the right-most optode is 10mm left to the right edge of the image. The (a), (b), and (c) correspond to the target depth of 17.5mm at longitudinal locations of 20, 40 and 60mm (counted from left edge), respectively. The (d), (e) and (f) correspond to the phantom depth of 12.5mm at longitudinal locations of 20, 40 and 60mm, respectively. The target is identified clearly against satisfactorily recovered background; however, the absorption contrast of the target is significantly underestimated.

The same data sets were reconstructed using the target spatial information obtained from TRUS. The TRUS image, similar to the one in Fig. 6(b), has artifacts around and shows only the lower half of the cylinder owing to the shadow effect. This image/artifact pattern is specific to the solid cylinder target that reflects much of the US signal on its surface. This type of artifact may not be representative for tissue imaging *in situ*. The artifact is thereby ignored when incorporating the spatial information of the target, by generating a mesh having a homogenous background region and a circular target region as shown in Fig. 6(c). As there are only two regions to reconstruct, the hierarchical iteration routine introduced in [1] involves only 2-steps. The results are given in Table 2 and Figure 9. The absorption coefficient of the background medium is reconstructed at 0.002mm^{-1} for all images. The absorption coefficient of the target is recovered to within 14% of the true value.

#99971 - $15.00 USD Received 8 Aug 2008; revised 13 Oct 2008; accepted 14 Oct 2008; published 15 Oct 2008

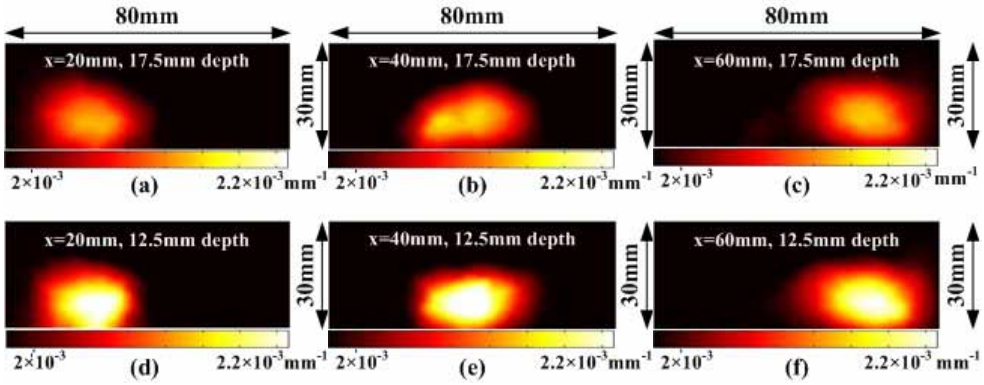

Fig. 8. NIR imaging of a solid tissue phantom having an absorption coefficient of 0.0056mm^{-1}. The reconstructed background absorption coefficients are 0.0019mm^{-1} in (a), (b), (d), (e), and 0.0020 mm^{-1} in (c), (f).

Table 2. NIR image reconstruction guided by TRUS- *prior*

Center depth	**12.5mm**		
Longitudinal location (x)	20mm	40mm	60mm
True Value (mm^{-1})	0.0056	0.0056	0.0056
Reconstructed value (mm^{-1})	0.0067	0.0064	0.0063
Center depth	**17.5mm**		
Longitudinal location (x)	20mm	20mm	20mm
True Value (mm^{-1})	0.0056	0.0056	0.0056
Reconstructed value (mm^{-1})	0.0064	0.0063	0.0061

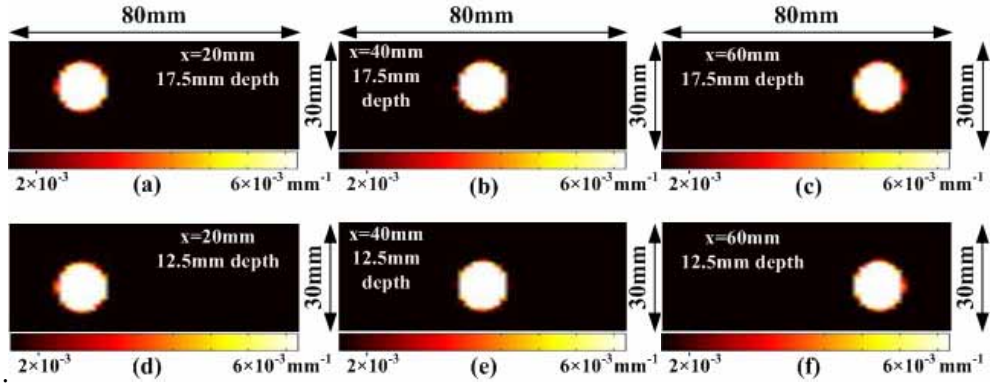

Fig. 9. TRUS guided NIR image reconstruction for solid phantom in homogenous medium

4.2 Imaging two targets

The capability of recovering more than one target by the endo-rectal NIR probe is also examined. Two cylinder-shaped solid tissue phantoms, including the one shown in Fig. 7(a), are used as the target. Both targets are 15mm in diameter and 25mm in length. The newly added solid phantom has an absorption coefficient of 0.0064mm^{-1} and a reduced scattering coefficient of 0.997 mm^{-1} in comparison to the other one of 0.0056mm^{-1} and 1.03mm^{-1}. Figure 10(a) and (b) are the images for placing the two targets at depths of 17.5mm and 22.5mm, respectively, in the mid-sagittal plane, with 20mm longitudinal spacing. When the reconstruction is performed without the target spatial information, the two targets can barely be differentiated at the depth of 17.5mm, and not discriminated at the depth of 22.5mm. The

#99971 - $15.00 USD Received 8 Aug 2008; revised 13 Oct 2008; accepted 14 Oct 2008; published 15 Oct 2008

absorption contrasts of the targets are also significantly underestimated in both cases. Figure 10(c) indicates the results of using the spatial information from the TRUS image. The two targets can be recovered as having different absorption contrasts, at both depths. The reconstructed absorption coefficients listed in Table 3 are also close to the true values.

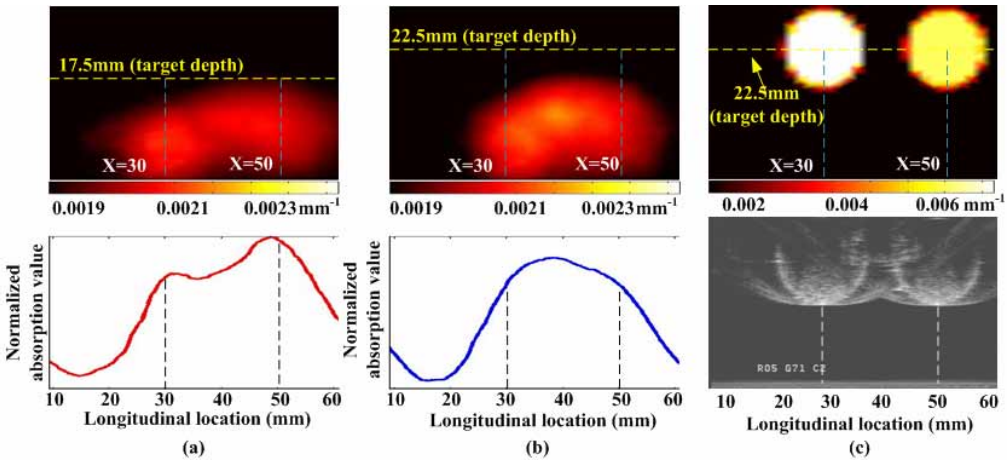

Fig. 10. Imaging of multiple targets: (a) NIR-only reconstruction when the target depth is 17.5mm, the targets can be barely separated; (b) NIR-only reconstruction when the target depth is 22.5mm, the targets cannot be separated; (c) region based reconstruction when the target depth is 22.5mm.

Table 3. Reconstructed absorption coefficients of the two targets in Fig. 12

	Target 1	Target 2
True value (mm^{-1})	0.0064	0.0056
Reconstructed value (mm^{-1})	0.0067	0.0058

4.3 Effects of condom on NIR tomography

The TRUS probe is always covered with a regular latex condom when imaging the prostate. A TRUS-coupled NIR applicator has to be applied with a condom if used in the clinic. In the previous applications of NIR tomography imaging there was no need of applying a latex barrier between an NIR applicator and the tissue being interrogated, therefore the effect of a latex condom on NIR tomography was not reported.

The test being carried out used the setup and solid phantom shown in Fig. 7, by applying US gel to the NIR/US probe, covering the NIR/US with a condom, then pressing the condom to eliminate any gas between the condom and the probe. US gel is not applied on top of the condom when imaging the Intralipid, but is applied for all the tissue imaging tests presented in Section 5. The absorption coefficient of the target reconstructed using TRUS information is listed in Table 4. The overall distribution of the reconstructed absorption coefficient of the target is plotted in Fig. 11(a), and the distribution specific to target position is plotted in Fig. 11(b). These results, which are consistent with those presented in Section 4.1, demonstrate that the condom has minimum effect on NIR imaging. Nevertheless, an attention of the light power is observed, as it takes 10% longer exposure time for CCD to integrate the same amount of signal when the condom is applied.

#99971 - $15.00 USD Received 8 Aug 2008; revised 13 Oct 2008; accepted 14 Oct 2008; published 15 Oct 2008

Table 4. Absorption coefficient reconstructed with the use of condom on the NIR probe (mm^{-1})

Depth (mm)	22.5	25	27.5	30	32.5	35	37.5
True value	0.0056	0.0056	0.0056	0.0056	0.0056	0.0056	0.0056
X=20mm	0.0065	0.0058	0.0070	0.0066	0.0048	0.0043	0.014
X=40mm	0.0053	0.0051	0.0047	0.0049	0.0043	0.0052	0.0063
X=60mm	0.0059	0.0045	0.0066	0.0052	0.0054	0.0095	0.0065

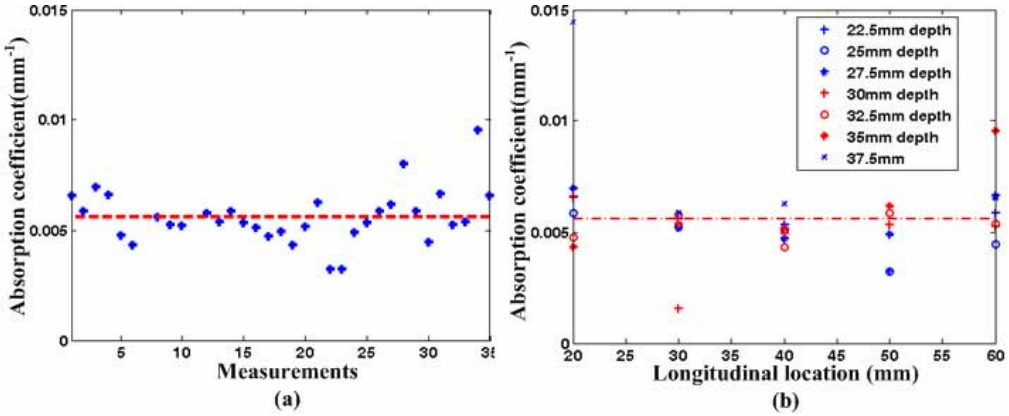

Fig. 11. Test of condom effect on the NIR imaging: (a) reconstructed absorption coefficients for all cases listed in Table 4, and The red dashed line shows the true value; (b) data points in (a) specific to target depths and longitudinal locations.

5. Results of tissue imaging by TRUS-coupled trans-rectal NIR tomography

5.1 Imaging solid absorbing object embedded in avian tissue

The condom-covered NIR/US probe was enclosed within thick layers of chicken breast tissue ($\mu_a = 0.006mm^{-1}$, $\mu_s' = 0.757mm^{-1}$ [35], and a black object (10mm diameter ×10mm length) was embedded as the target. The photographs in Fig. 12(a) and (b) show the setup of tissue sample and the absorbing target being embedded. The tissue without the absorbing target is also imaged as a baseline test. The baseline images by US and NIR are shown in Fig. 12(c), where the NIR image is reconstructed using a homogenous mesh as there was no indication of a target on US. Figure 12(d) to (f) correspond to target being embedded at different longitudinal locations at slightly different depths. The embedded object is clearly visible in the US images as anechoic shadows. The NIR imaging without prior information can clearly recover the object, but with inconsistent and potentially much under-estimated absorption coefficients. When the target location and size information are used to guide the NIR image reconstruction, the target is recovered with consistent absorption coefficients indicating a strongly absorbing object.

5.2 Internal imaging of avian tissues

As shown in Fig. 13(a) the empty abdomen of a whole chicken was filled with chicken breast tissue and a piece of chicken liver was embedded within the breast tissue. The embedded liver shows up as the hypo-echoic region circled in Fig. 13(b). The NIR image reconstructed without any target information is given in Fig. 13(c), in which the absorptive mass does correlate longitudinally with the liver tissue. Fig. 13(d) shows NIR image reconstructed by treating the liver mass as a sphere. Fig. 13(e) shows the NIR image reconstructed by excluding the non-tissue region from the background of Fig. 13(b). Fig. 13(f) shows the NIR

#99971 - $15.00 USD Received 8 Aug 2008; revised 13 Oct 2008; accepted 14 Oct 2008; published 15 Oct 2008

image reconstructed by taking into account the irregular shape of the liver mass. Among the 3 spatial *prior* implementations, the one in Fig. 13(f) is the most accurate wherein the absorption coefficient of the chicken liver mass is also the closest to the realistic value [35].

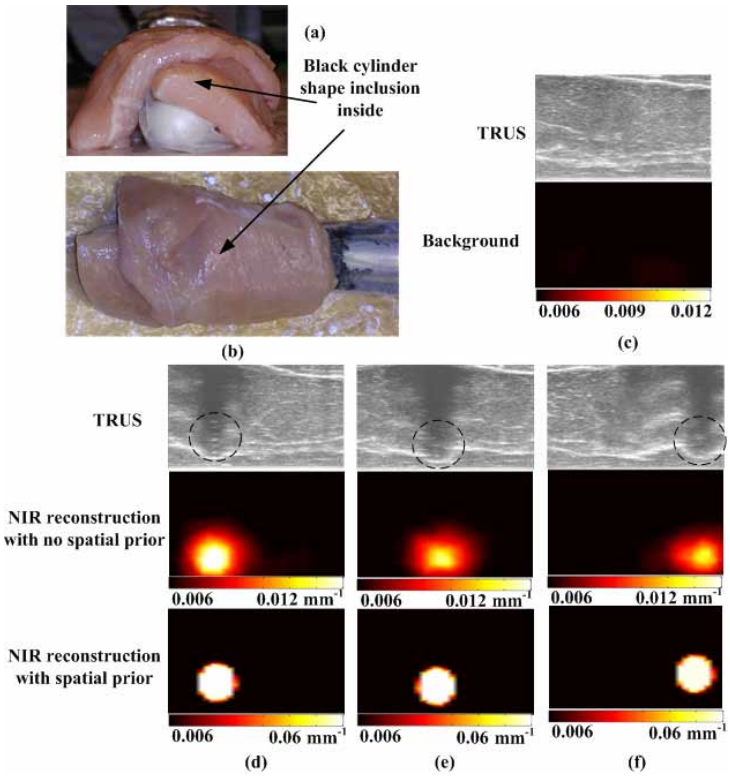

Fig. 12. Avian tissue imaging: (a) front view; (b) top view; (c) no inclusion; (d) inclusion is at 20mm; (e) 35mm; (f) 58mm, longitudinally, respectively.

5.3 TRUS-coupled trans-rectal optical tomography of canine prostate in situ

TRUS-coupled trans-rectal NIR imaging of the prostate is conducted on a canine cadaver. The prostate was exposed and approximately 0.33ml of homogenized foal liver was injected ventral-dorsally, paramedian in the left lobe of the prostate. The prostate was then enclosed in thick layers of peri-prostate tissues. On the TRUS image of Fig. 14(a) the injected liver tissue is visible by the mass proximal to the center of the prostate and the vertical hyper-echoic strip at the ventral side of the prostate. The large hypo-echoic region at the upper half was due to air. The mesh generated in Fig. 14(b) has excluded the air based on the US image. The rectum wall was not outlined in the mesh because of its close proximity and near apposition to the US transducer due to the small size of this canine cadaver. The rectum layer may be included when imaging a larger subject. The finalized mesh given in Fig. 14(b) shows nested-domains where there is a relatively small prostate and a much smaller target in the prostate. The NIR image in Fig. 14(c) is reconstructed by applying the 3-step hierarchical reconstruction method introduced in the previous paper [1]. A highly absorptive mass is clearly recovered out of the injected liver tissue. The absorption coefficient of the foal liver tissue in Fig. 14(c) is lower than that of the avian liver tissue in Fig. 13(f); nevertheless both values are at the order of $0.1mm^{-1}$, indicating high absorption by both tissues. The reconstructed absorption coefficients of the prostate and the peripheral tissue are given in Table 5. It is very interesting to observe that the numbers agree with the values suggested by the literature [16-18, 35].

#99971 - $15.00 USD Received 8 Aug 2008; revised 13 Oct 2008; accepted 14 Oct 2008; published 15 Oct 2008

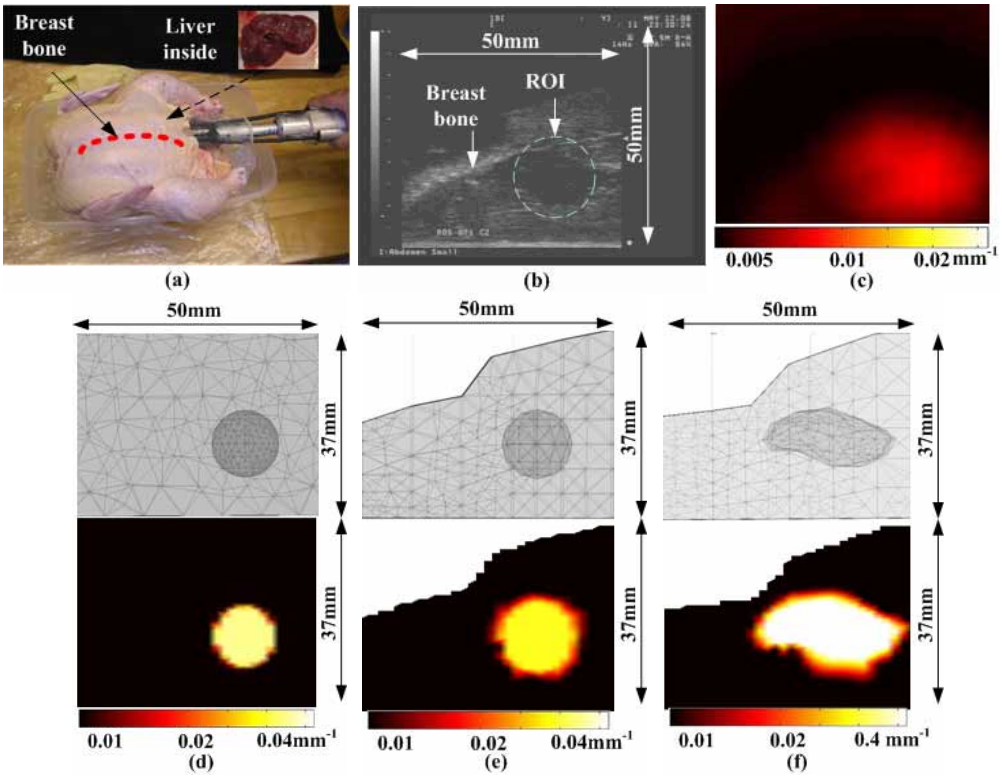

Fig. 13. Internal imaging of avian tissue embedded with a piece of liver. (a) Whole chicken sample; (b) US image of the embedded liver tissue; (c) NIR image reconstructed without US *prior*; (d) NIR image reconstructed assuming a circular target; (e) NIR image reconstructed by adding the boundary profile of the background tissue; (f) NIR image reconstructed by adding the actual contour of the target.

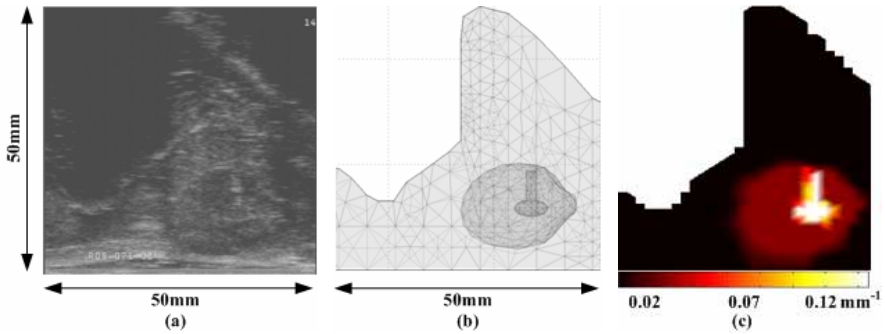

Fig.14. Trans-rectal NIR / US imaging of in vitro canine prostate with exogenous tissue contrast.

Table 5 Reconstructed absorption value of in vitro canine prostate imaging

Region	Background	Prostate	Injected liver
Reconstructed value (mm^{-1})	0.0062	0.0309	0.1301

6. Discussion

In the NIR imager an 840nm superliminescent diode with ~14nm bandwidth is used to simultaneously excite all source channels. The bandwidth would certainly introduce

#99971 - $15.00 USD Received 8 Aug 2008; revised 13 Oct 2008; accepted 14 Oct 2008; published 15 Oct 2008

wavelength-dependent attenuation among source channels for the same tissue chromophore. The reconstructed absorption coefficient is therefore a value averaged over the band coupled into the source channels. Luckily the absorption of the tissue chromorphores like hemoglobin is less wavelength-dependent in the close vicinity of 840nm. If the source coupling method is performed at an additional wavelength, such as 780nm, to quantify the oxygen saturation [36], it may be necessary to compensate the wavelength-dependent absorptions among source channels in image reconstruction.

It is shown that the absorption coefficient can be quantitatively reconstructed by steady-state trans-rectal NIR measurements. The accuracy of reconstruction for a highly heterogeneous domain can be improved dramatically by use of the TRUS spatial *prior*. Implementing frequency-domain detection to the NIR system will also allow more accurate reconstruction of the absorption coefficient owing to the reliable differentiation of it from the scattering by true phase information.

Generating the target mesh from the TRUS image has been based on the assumption that the entire imaging volume and the target are symmetric and centered at the TRUS imaging plane. This is perhaps necessary if only one TRUS image is utilized to form a 3-dimensional mesh for NIR image reconstruction, but is mostly inaccurate. This is particularly problematic in imaging of the prostate if the NIR/US probe is to be directed away from the midline of the prostate. The effect of asymmetric-domain may be corrected if multiple US images are available to generate a mesh representing the true 3-dimensional contents of the imaging volume more faithfully.

The trans-rectal examination of the prostate on the sagittal view is likely being interfered with by the nearby bladder and pelvic bone. If the bladder is empty, the photon propagation may be less interrupted. If the bladder is full, it may become a relatively transparent domain for photon propagation. In this case the bladder likely becomes a diffusion-void domain [37, 38]. A transport-equation based model of photon propagation can be implemented [37, 39] to mitigate the interference of void-domains. The interference from the pelvic bone is similar in principle to that of the chest wall in breast imaging when using a planner NIR array [40]. In this work we applied the Robin-type boundary condition under diffusion equation to the void-tissue interfaces under the diffusion model. This is a rather straightforward approach that is proven helpful for improving the reconstruction accuracy, but more studies are needed to quantitatively evaluate improvement by this approach in comparison to the more rigorous transport-based model.

The probe sensitivity curves in this paper and those in the previous paper [1] were all derived under the assumption of an absorptive NIR probe surface. This boundary condition produces a peak of depth-sensitivity close to, but not at, the probe surface. This feature may be desirable for prostate imaging, since the measurement will be less sensitive to the existence of a rectum layer. On the other hand, the peak also indicates that the measurement is less sensitive to a lesion deeper in the prostate than one closer to the surface of the prostate. Prostate tumors are known to occur more often in the peripheral zone which stretches abaxial from the middle-line of the prostate. For deeper target, we have showed that with TRUS *prior*, the accuracy of target recovery can be improved successfully. However, more dedicated simulation and experimental studies are necessary to evaluate the likelihood of retrieving deeper target *in vivo*.

In all the tests presented in this work, the target of interest is visible or at least sensitive to US, therefore US spatial information of the target is readily rendered to guide the NIR image reconstruction. If the target is ambiguous to US, it may still be recognizable by NIR-only reconstruction. One example is given in Fig. 15 wherein a piece of chicken breast tissue was dyed with diluted Indian ink and then placed in the middle of the natural chicken breast tissue. The approximate boundary of the dyed tissue is marked with the dash-circle in the US image. This embedded tissue is hardly distinguishable in the TRUS image; therefore the NIR image reconstruction was performed without any a *priori* information. The target is identified by

#99971 - $15.00 USD Received 8 Aug 2008; revised 13 Oct 2008; accepted 14 Oct 2008; published 15 Oct 2008

NIR even though the depth and size were not accurate. This result may show positive indication on the clinical application of trans-rectal NIR/US measurement providing the fact that up to 40% of prostate tumors are not sensitive to US [3, 6, 7]. Besides using NIR information to characterize US-sensitive lesions, if the NIR imaging is able to discover a lesion that is otherwise non-suspicious on US, the overall sensitivity and specificity of TRUS-based prostate imaging may be improved.

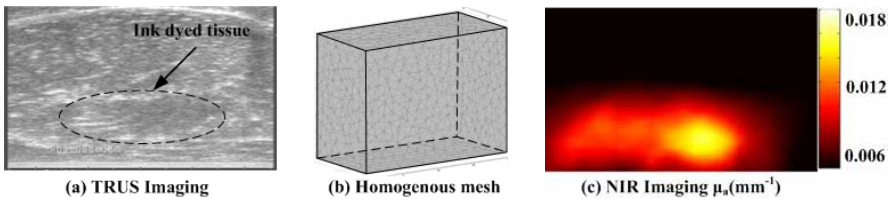

Fig. 15. Imaging of a tissue mass that is ambiguous to TRUS but sensitive to NIR.

7. Conclusions

We implemented the NIR array design suggested in our previous work for direct integration of the NIR array with a TRUS transducer. The combined NIR/US probe & system enabled concurrent acquisition of trans-rectal NIR tomography and TRUS images in the same sagittal plane. Although the NIR imager is constructed in CW mode, accurate quantitative reconstruction of the absorption coefficient is feasible with the TRUS spatial *a priori* information. The use of a condom is found to have minimum affect on NIR tomography measurement, indicating that endo-rectal NIR may be applied concurrently with TRUS in a clinic setting with no alteration of the standard procedures. An absorptive target may also be recovered by trans-rectal NIR only, but the incorporation of TRUS *a priori* information allows trans-rectal NIR tomography to recover an absorption target more accurately, as demonstrated by imaging of the alien tissue in the canine prostate. The previous Part-I and this Part-II papers together have validated prostate imaging as feasible by TRUS-coupled trans-rectal NIR tomography. Work is on-going toward *in vivo* measurement of optical properties in intact prostate as well as development of prostate cancer models in the canine to validate that augmenting TRUS morphology information with trans-rectally acquired NIR contrast may improve the overall accuracy of TRUS prostate imaging.

Acknowledgments

This work has been supported by the Prostate Cancer Research Program of the U.S. Army Medical Research Acquisition Activity (USAMRAA), 820 Chandler Street, Fort Detrick MD, 21702-5014, through grant #W81XWH-07-1-0247. The content of the information does not necessarily reflect the position or the policy of the USARAA, and no official endorsement should be inferred. The authors would like to thank Drs. Brian W. Pogue and Quing Zhu for enlightening discussions and suggestions. Comments and questions may be directed to Daqing Piao whose e-mail address is daqing.piao@okstate.edu.

#99971 - $15.00 USD Received 8 Aug 2008; revised 13 Oct 2008; accepted 14 Oct 2008; published 15 Oct 2008